Available online at www.sciencedirect.com
ScienceDirect
Journal of the European Ceramic Society 30 (2010) 3209–3217
www.elsevier.com/locate/jeurceramsoc

Oxidation behaviour of pressureless liquid-phase-sintered α-SiC with additions of $5Al_2O_3 + 3RE_2O_3$ (RE = La, Nd, Y, Er, Tm, or Yb)

F. Rodríguez-Rojas [a], A.L. Ortiz [a,*], F. Guiberteau [a], M. Nygren [b]

[a] *Departamento de Ingeniería Mecánica, Energética y de los Materiales, Escuela de Ingenierías Industriales, Universidad de Extremadura, 06071 Badajoz, Spain*
[b] *Department of Material and Environmental Chemistry, Arrhenius Laboratory, University of Stockholm, 10691 Stockholm, Sweden*

Received 17 February 2010; received in revised form 6 July 2010; accepted 6 July 2010

Abstract

The oxidation behaviour of pressureless liquid-phase-sintered (PLPS) α-SiC was investigated as a function of the sintering additives of $5Al_2O_3 + 3RE_2O_3$ (RE = La, Nd, Y, Er, Tm, or Yb) by thermogravimetry experiments in oxygen at 1075–1400 °C for up to 22 h. It was found that the oxidation is in all cases passive and protective, with kinetics governed by the arctan-rate law. This is because the PLPS SiC ceramics develop oxide scales having no cracks or open porosity and accordingly prevent the parent material from direct contact with oxygen. In addition, these oxide scales crystallize gradually during the exposure to the oxidizing atmosphere with the attendant reduction in the amorphous cross-section available for oxygen diffusion. It was also found that the rate-limiting mechanism of the oxidation is outward diffusion of RE^{3+} cations from the intergranular phase into the oxide scale, and that the activation energy of the oxidation increases with increasing size of the RE^{3+} cation. It was also observed that the oxidation of PLPS SiC increases with increasing size of the RE^{3+} cation, an effect that is especially marked for cation sizes above 0.9 Å because the oxidation rate becomes several orders of magnitude faster. This trend is attributable to the oxide scales being more crystalline, and containing crystals that are more refractory and amorphous residual phases that are more viscous as the size of the RE^{3+} cation decreases. Finally, implications for the design of PLPS SiC ceramics with superior oxidation resistance are discussed.

Keywords: SiC; Liquid-phase sintering; Oxidation; Corrosion; Diffusion

1. Introduction

SiC is an important advanced ceramic with a wide variety of applications in numerous technological industries. Owing to its covalent bonding and low self-diffusion coefficients, SiC is typically densified by liquid-phase sintering with the help of metal-oxide additives. The commonest of these additives is $5Al_2O_3 + 3Y_2O_3$, but other combinations of Al_2O_3 or AlN with Y_2O_3 or other rare-earth oxides (RE_2O_3) are equally effective in densifying SiC.[1,2] A particularly important aspect of liquid-phase-sintered (LPS) SiC is that its microstructure necessarily contains second phases at grain boundaries and triple points. In consequence, the choice of the sintering additives will affect many of its properties as a structural material. One of these important properties is its oxidation resistance because LPS SiC is a non-oxide ceramic whose oxidation proceeds not only by inward diffusion of oxygen to form SiO_2, but also by outward diffusion of metal cations from the intergranular phase and their subsequent reaction with part of the formed SiO_2 to produce crystalline and vitreous metal-silicates.[3–11] These results indicate that the oxidation of LPS SiC is complex and likely to change with the intergranular phase chemistry. Indeed, this expectation has been confirmed in two studies. Weidenmann et al.[9] oxidized three LPS SiCs fabricated by gas-pressure sintering with 10 vol.% $AlN + Lu_2O_3$, $AlN + Y_2O_3$, or $Ho_2O_3 + Lu_2O_3$ at 1400 °C in wet air, and found that the oxidation resistance decreased with increasing cationic radius of the sintering aids. Choi et al.[12] observed the same trend in three LPS SiCs fabricated by hot-pressing plus gas-pressure sintering with 10.5 vol.% $AlN + Y_2O_3$, $AlN + Er_2O_3$, or $AlN + Yb_2O_3$, and then oxidized at 1400 °C in air.

Although these two proof-of-concept studies are very interesting, there are several issues that need to be resolved. In particular, neither of them was carried out on pressureless (P)

* Corresponding author.
E-mail address: alortiz@unex.es (A.L. Ortiz).

0955-2219/$ – see front matter © 2010 Elsevier Ltd. All rights reserved.
doi:10.1016/j.jeurceramsoc.2010.07.013

LPS SiCs with Al_2O_3 as one of the sintering additives, and they both measured the oxidation behaviour for only three combinations of sintering additives and one oxidizing temperature which does not allow the rate-controlling mechanism and activation energy of the oxidation to be determined. This underscores the necessity of including more combinations of sintering additives and more oxidizing temperatures in a systematic oxidation study on a PLPS SiC.

With these premises in mind, the present study was undertaken with the objective of investigating in more detail the sintering-additive dependence of the oxidation behaviour of PLPS SiC with simultaneous additions of Al_2O_3 and RE_2O_3 (RE = La, Nd, Y, Er, Tm, or Yb), including the evaluation of the kinetic model, activation energy, and rate-controlling mechanism of the oxidation as a function of cationic radius in the RE_2O_3. Finally implications for optimizing the processing route of PLPS SiC for oxidation-resistance applications will be discussed.

2. Experimental procedure

Fully dense PLPS SiC ceramics were prepared from six powder batches each containing α-SiC (UF-15, H.C. Starck, Goslar, Germany), plus Al_2O_3 (AKP-30, Sumitomo Chemical Company, NY) and RE_2O_3 (RE = La, Nd, Y, Er, Tm, or Yb) in 5:3 molar ratio as sintering additives. The relative amounts of SiC and ($5Al_2O_3 + 3RE_2O_3$) in each of the powder batches were designed to yield in all cases PLPS SiC ceramics with 90 vol.% SiC and 10 vol.% $RE_3Al_5O_{12}$ after sintering (abbreviated hereafter as PLPS SiC–RE). The powder batches were prepared using routine methods applicable to ceramic materials, that is, by successive steps of powder wet mixing/homogenization, drying of the slurries under stirring, and deagglomeration by crushing.[13] Compacts were made by uniaxial pressing (C, Carver Inc., Wabash, IN, USA) at 50 MPa, followed by isostatic pressing (CP360, AIP, Columbus, OH, USA) at 350 MPa. Pressureless sintering was performed in a graphite furnace (1000-3560-FP20, Thermal Technology Inc., Santa Rosa, CA, USA) at 1950 °C for 1 h in a flowing Ar-gas atmosphere of 99.999% purity.

The oxidation tests were carried out with a thermobalance (TAG 24, Setaram, France), and parallelepiped specimens of size 8 mm × 5 mm × 2 mm with all their faces diamond-polished to a 1-μm finish were attached to the balance via a Pt wire. The resolution of the thermobalance used is better than 2 μg, and the baseline drift lower than 5 μg per 24 h. The oxidation tests were performed at temperatures ranging between 1075 and 1400 °C, in an atmosphere of flowing (50 mL/min) dry oxygen of 99.999% purity, and for times in the range 0–22 h.

The as-processed and oxidized samples were characterized by scanning electron microscopy (SEM; S-3600N, Hitachi, Japan), energy dispersive X-ray spectroscopy (EDXS; XFLASH Detector 3001, Röntec GmbH, Germany), and X-ray diffractometry (XRD; X'pert PRO MPD, PANalytical, The Netherlands). The SEM observations of the as-processed samples were made on cross-sectional specimens polished to a 1-μm finish, then plasma etched with CF_4 + 4% O_2 gas for 2 h, and finally metallized with Pt, whereas the SEM examinations of the oxidized samples were made on plane-view specimens only metallized and on cross-sectional specimens first polished to a 1-μm finish and then metallized. In all cases the SEM micrographs were taken at 30 kV with backscattered electrons (BSE). The EDXS compositional maps were taken in the SEM at 15 kV, using the same cross-sectional specimens used for the SEM observations. The XRD analyses were always made on plane-view specimens, and were collected in the step scanning mode (2θ in the range 20–100°, step width 0.0263°, and count time 2 s per step) using Cu-Kα_1 incident radiation. The XRD patterns were indexed using the PDF2 database.

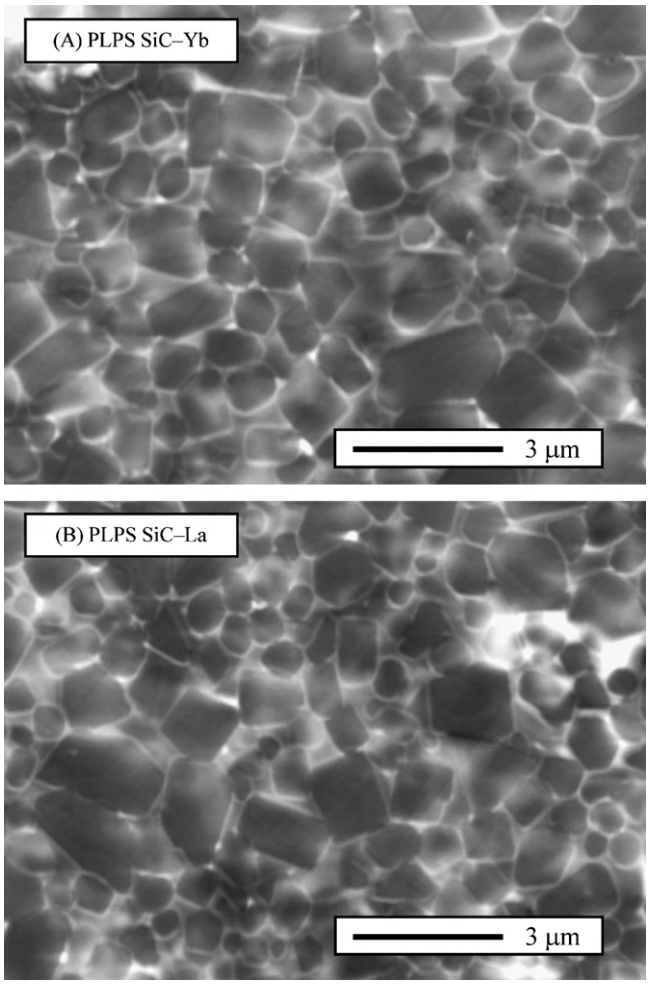

Fig. 1. BSE-SEM micrographs of the PLPS SiC ceramics fabricated with the smallest and largest RE^{3+} cations in the RE_2O_3 used as sintering aid together with Al_2O_3: (A) PLPS SiC–Yb (Yb^{3+} radius 0.868 Å), and (B) PLPS SiC–La (La^{3+} radius 1.032 Å). The dark regions are the SiC grains and the light region is the $RE_3Al_5O_{12}$ phase.

3. Results

3.1. Microstructure of the as-processed samples

Fig. 1 compares representative SEM images of the microstructure of PLPS SiC–La and PLPS SiC–Yb, that is, of the samples prepared with the lanthanoids of smallest (Yb^{3+})

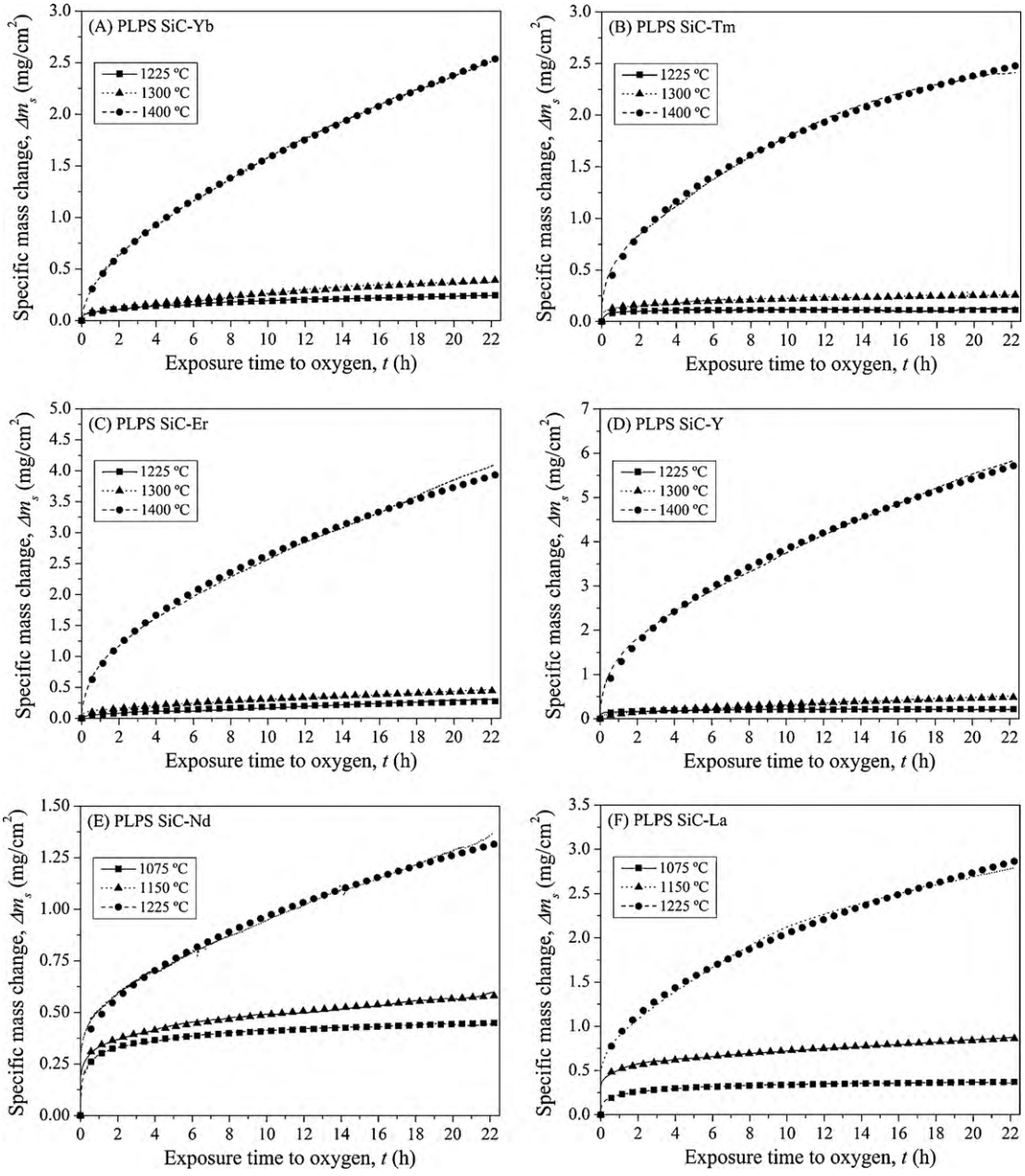

Fig. 2. Oxidation curves in oxygen of the six ceramics prepared in this study: (A) PLPS SiC–Yb, (B) PLPS SiC–Tm, (C) PLPS SiC–Er, (D) PLPS SiC–Y, (E) PLPS SiC–Nd, and (F) PLPS SiC–La. The lines are the experimental data, and the points are the arctan models of the oxidation kinetics (discussed in the text).

and largest (La^{3+}) cationic radius. As can be observed, the microstructure is independent of the RE_2O_3 used in combination with Al_2O_3, a fact that the SEM analyses on the rest of samples (i.e., PLPS SiC–Tm, –Er, –Y, and –Nd) confirmed. In particular, the SiC grains have the same equiaxed form (aspect ratio ~1.4) and submicrometre size (~0.8 μm), and are always embedded within an intergranular phase that according to XRD is crystalline $RE_2Al_5O_{12}$.

3.2. Oxidation kinetics

Fig. 2 shows the specific mass-change curves for the six PLPS SiC–RE ceramics oxidized in dry oxygen in the temperature range 1075–1400 °C. As can be observed, regardless of the $5Al_2O_3 + 3RE_2O_3$ combination, there is always mass gain throughout the oxidation period, with a kinetics that does not obey the linear-rate law. In addition, the $(\Delta m_s)^2$-t plots are not linear either but exhibit a certain concavity (not shown), indicating that the oxidation kinetics does not obey the typical parabolic-rate law either. There are two rate laws that in principle can account for the concavity of the $(\Delta m_s)^2$-t plots. One is the paralinear-rate law, which incorporates two terms, one positive for the growth of the oxide scale (i.e., $(k_p t)^{1/2}$) and the other negative for its recession (i.e., $-k_l t$)[9,14,15]; the other is the arctan-rate law, which considers that the effective diffusion rate is time-dependent due to the gradual reduction in the amorphous cross-section available for oxygen diffusion induced by the pro-

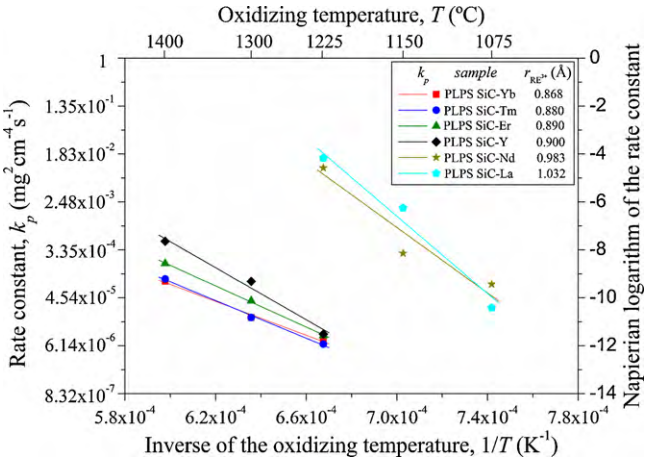

Fig. 3. The oxidation rate constants (k_p) for the six PLPS SiC–RE ceramics as a function of temperature, and the corresponding Arrhenius plot. The points are the k_p values determined by the arctan oxidation kinetics model, and the lines are the best linear fits to the Arrhenius expression.

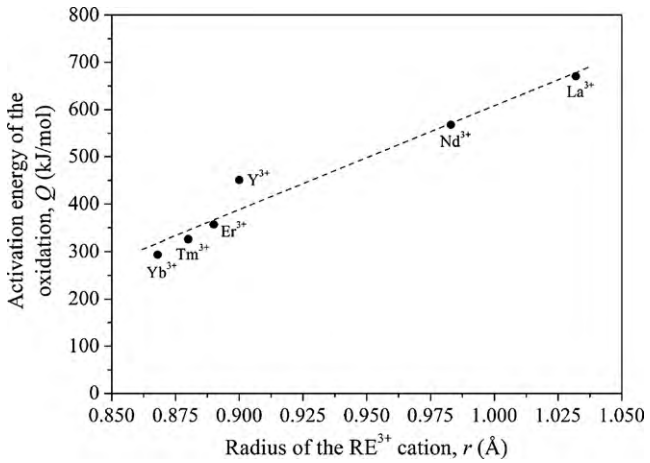

Fig. 4. The activation energy (Q) of the oxidation for the PLPS SiC ceramics as a function of size of the RE^{3+} cation in the RE_2O_3 used as sintering aid together with Al_2O_3. The points are the Q values determined by the Arrhenius expression, and the dashed line is to guide the eyes.

gressive crystallization of the oxide scale during oxidation[14,16] (see Appendix A for details). However, modeling the oxidation kinetics with a paralinear-rate law did not lead to satisfactory fits, and was therefore ruled out. The oxidation curves were then modelled using the arctan-rate law in the form:

$$\Delta m_s = \frac{\beta\sqrt{K_p}(1-f)}{\sqrt[3]{(\beta-1/t_0)^2}} \arctan\sqrt{(\beta-1/t_0)t} + \frac{\sqrt{K_p}(\beta f-1/t_0)}{(\beta-1/t_0)}\sqrt{t}+b \quad (1)$$

where Δm_s is the specific mass variation (weight change per surface area), k_p the parabolic-rate constant, β the rate constant for the decrease of the area, f the fraction of original area that still remains amorphous, t_0 the time at which the crystallization process stops, and b an additive constant (ideally equal to zero) that accounts for the possible mass change at the beginning of the isothermal oxidation test ($t=0$). As can be observed in Fig. 2, the model oxidation curves calculated by Eq. (1) (see Appendix B for details) describe the experimentally-measured oxidation curves remarkably well (i.e., $r>0.9$).

Fig. 3 compares the oxidation rate constants for the six PLPS SiC–RE ceramics. The following three observations can be made. First, k_p decreases with decreasing size of the RE^{3+} cation, a trend that is more pronounced as the oxidizing temperature increases. Second, two groups of materials are identified in the sense that the k_p values rise by several orders of magnitude when the size of the RE^{3+} cation reaches ~0.9 Å. And third, the k_p constants of PLPS SiC–Yb, –Tm, –Er, and –Y seem to converge to a common value at approximately 1200 °C. It is also observed in Fig. 3 that $Ln\ k_p$ seems to be directly proportional to $1/T$, as predicted by the Arrhenius expression $Ln\ k_p = Ln\ k_{p,0} - Q/RT$, where $k_{p,0}$ is the pre-exponential factor, R is the universal gas constant (8.314 J/mol K), and Q is the activation energy of the oxidation. The corresponding best fit lines are shown in Fig. 3, and the resulting activation energies are plotted in Fig. 4 as a function of radius of the RE^{3+} cation. As can be observed, the activation energy for the oxidation of PLPS SiC decreases from 671 ± 117 to 294 ± 23 kJ/mol with decreasing size of the RE^{3+} cation from 1.032 (La^{3+}) to 0.868 Å (Yb^{3+}).

3.3. Microstructure of the oxidized samples

Fig. 5 compares representative cross-sectional SEM images of the PLPS SiC ceramics prepared with the RE^{3+} cations of extreme size (i.e., Yb^{3+} and La^{3+}) after a similar degree of oxidation. As can be observed, in both cases the oxidation products formed a continuous condensed phase on the sample surface, the oxide scales are free of cracks or open porosity, and there is a composition contrast below the oxide scale. Detailed compositional mappings by XEDS in the SEM, such as those shown in Fig. 6, reveal that this compositional contrast is due to the formation of a zone depleted of RE^{3+} cations immediately below the oxide scale.

It is also very clear in Figs. 5 and 6 that the oxide scale in PLPS SiC–Yb, which has the smallest RE^{3+} cation, is markedly crystalline (the crystals being rich in Yb), whereas the oxide scale in PLPS SiC–La, which has the largest RE^{3+} cation, is manifestly more vitreous and porous despite the lower oxidizing temperature. As shown in Fig. 7, the plane-view SEM observations of the oxide scale in the six PLPS SiC–RE ceramics oxidized at 1225 °C[a] for 22 h confirm that the closed porosity decreases and the crystallinity increases with decreasing size of the RE^{3+} cation in the RE_2O_3. The high compositional contrast in the BSE-SEM images (atomic number contrast) of Fig. 7 indicates that the crystals are lanthanoid-rich phases. In particular, the XRD analyses of the six PLPS SiC–RE ceramics revealed that these crystals are indeed rare-earth di-silicates (i.e., $RE_2Si_2O_7$), and that the oxide scales also contain crystalline SiO_2. Furthermore, they also showed that, for the same oxi-

[a] 1225 °C was chosen for the comparison because this oxidizing temperature was shared by all samples.

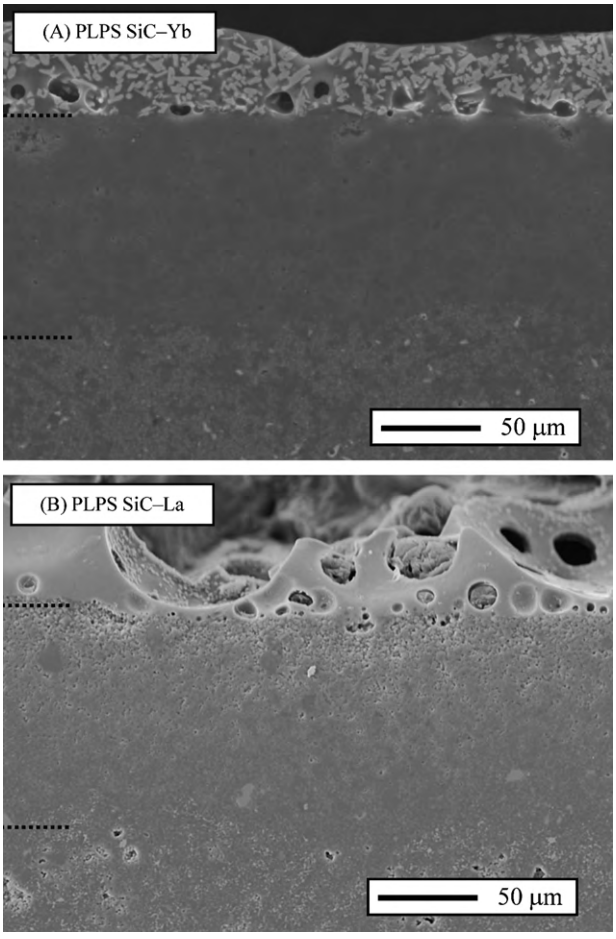

Fig. 5. Cross-sectional BSE-SEM micrographs of the PLPS SiC ceramics fabricated with the smallest and largest RE^{3+} cations after a similar degree of oxidation in oxygen for 22 h: (A) PLPS SiC–Yb (Yb^{3+} radius 0.868 Å) oxidized at 1400 °C, and (B) PLPS SiC–La (La^{3+} radius 1.032 Å) oxidized at 1225 °C. The dotted lines indicate the thickness of the region depleted of RE^{3+} cations.

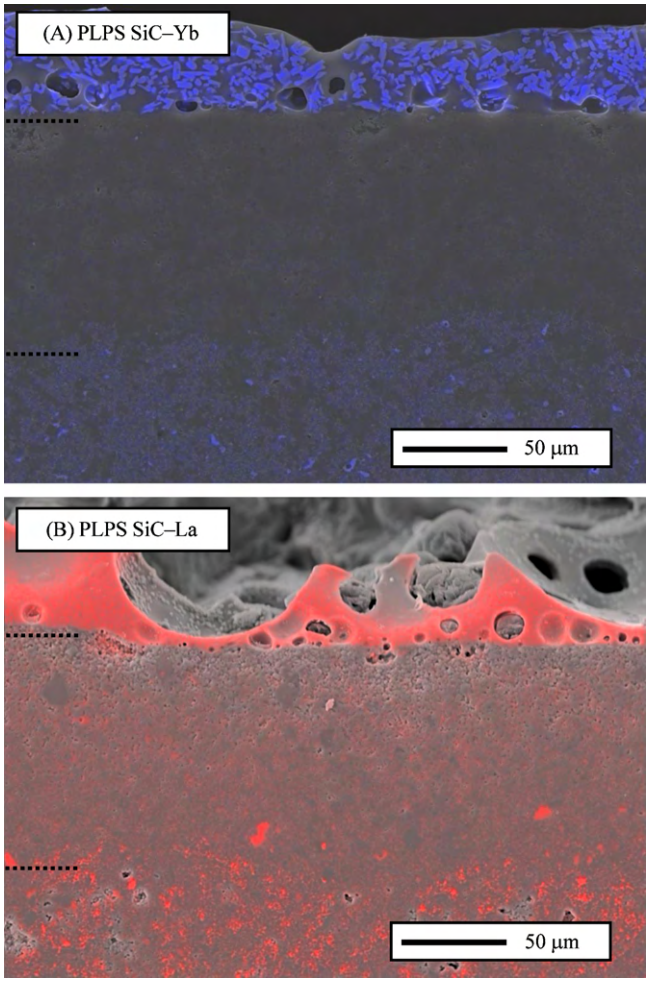

Fig. 6. Compositional mapping of the corresponding RE element in the cross-sectional BSE-SEM micrographs of Fig. 5: (A) PLPS SiC–Yb and (B) PLPS SiC–La. See caption of Fig. 5 for more details.

dizing temperature, the oxide scales are more crystalline as the size of the RE^{3+} cation decreases. By way of example, Fig. 8 shows these features for selected samples (see the peak indexing for the as-processed and oxidized PLPS SiC–Yb, and that after oxidation at 1225 °C there are more peaks and the peak-to-background ratio is much higher in PLPS SiC–Yb than in PLPS SiC–La).

Thus, taken together, the SEM, XEDS and XRD analyses indicate that the oxidation of the PLPS SiC–RE ceramics is complex involving various chemical reactions, and that the growth of the oxide scale occurs by counter-diffusion of oxygen inward and of RE^{3+} cations outward. In particular, the formation of SiO_2 via oxidation of the SiC grains is accompanied by the reaction of part of the so-formed SiO_2 with the secondary intergranular phase to form metal-silicates. The subsequent outward migration of metal cations from the parent material towards the oxide scale to continue the formation of silicates results in a zone depleted of metal cations immediately below the oxide scale.

4. Discussion

The results presented above indicate that, regardless of the $5Al_2O_3 + 3RE_2O_3$ combination used as sintering aid, the oxidation of PLPS SiC is passive and protective, and is controlled by diffusion of RE^{3+} cations. The former of these conclusions is derived from observations of oxide scales on the surface of the oxidized samples (see Figs. 5 and 7) and of non-linear oxidation kinetics with mass gains (see Fig. 2), because in active oxidation the oxidation products are all gaseous and therefore the sample loses mass and does not develop oxide scale.[14] The latter of these conclusions is inferred from several observations. First, the oxidation kinetics obeys the arctan-rate law, which is derived from Fick's first law of diffusion assuming that the oxide scale crystallizes progressively during the exposure to the oxidizing atmosphere.[16] The formation of oxide scales that are free of cracks or open porosity (see Fig. 5) and the depletion of RE^{3+} cations just below the oxide scale (see Fig. 6) are consistent with the oxidation being controlled by a diffusion process.[10,14] Second, the activation energies determined by the Arrhenius plots (see Fig. 4) are greater than the typical activation energy associated with the inward diffusion of oxygen through SiO_2

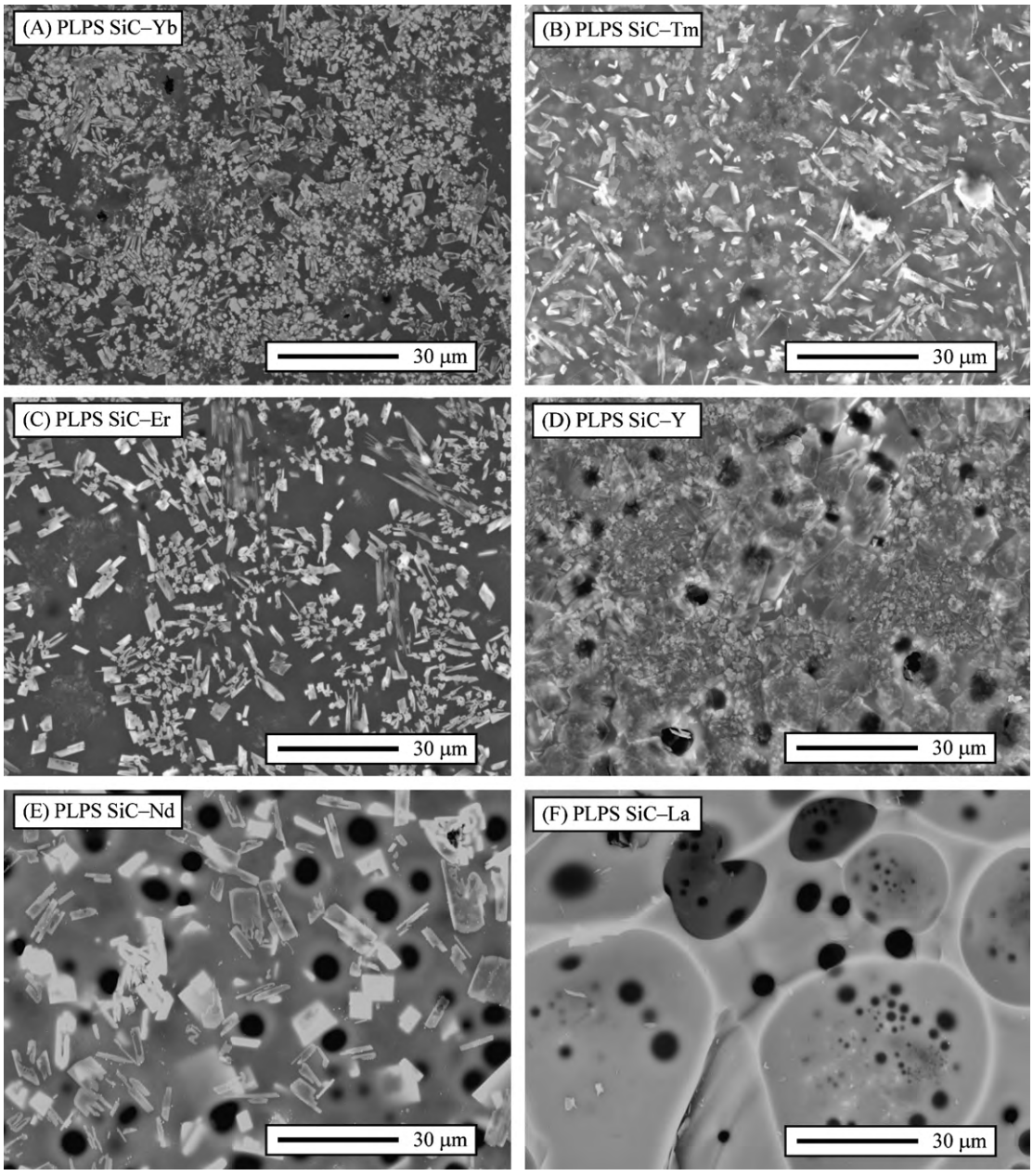

Fig. 7. Plane-view BSE-SEM micrographs the six ceramics prepared in this study after oxidation at 1225 °C in oxygen for 22 h: (A) PLPS SiC–Yb, (B) PLPS SiC–Tm, (C) PLPS SiC–Er, (D) PLPS SiC–Y, (E) PLPS SiC–Nd, and (F) PLPS SiC–La.

(∼150 kJ/mol) or multicomponent SiO_2 (∼250 kJ/mol) layers,[14] indicating that the rate-limiting mechanism of the oxidation is outward diffusion of cations from the secondary intergranular phase into the oxide scale. Note that the metal cations render inward diffusion of oxygen faster by five or more orders of magnitude[17] because they reduce notably the viscosity of the silicate liquid, and therefore they enable oxidation to take place more easily. Outward diffusion of cations is thus a necessary step in the short-term oxidation of PLPS SiC, and is slower than inward diffusion of oxygen. And third, the large variation in the activation energies between the different samples, which all have Al^{3+} cations in common but differ in RE^{3+} cations, indicates that the rate-limiting mechanism is diffusion of RE^{3+} cations. With this rate-limiting mechanism, the activation energy decreases from 671 ± 117 for PLPS SiC–La to 294 ± 23 kJ/mol for PLPS SiC–Yb (see Fig. 4) because the diffusion of the RE^{3+} cations is easier as their size decreases.[18]

The results also showed that which RE_2O_3 is used in combination with Al_2O_3 does affect the oxidation resistance of the PLPS SiC which increases with decreasing size of the RE^{3+} cation (see Fig. 3). This is because the oxide scale becomes less permeable to the diffusion of oxygen due to the combination of its greater crystallinity, greater refractoriness of its crystals, and greater viscosity of its amorphous residual phase. The greater crystallinity of the oxide scale is attributable to the easier diffusion of the smaller RE^{3+} cations favouring the formation of metal-silicates, which logically helps to improve the oxidation resistance because the oxygen diffusion rate through

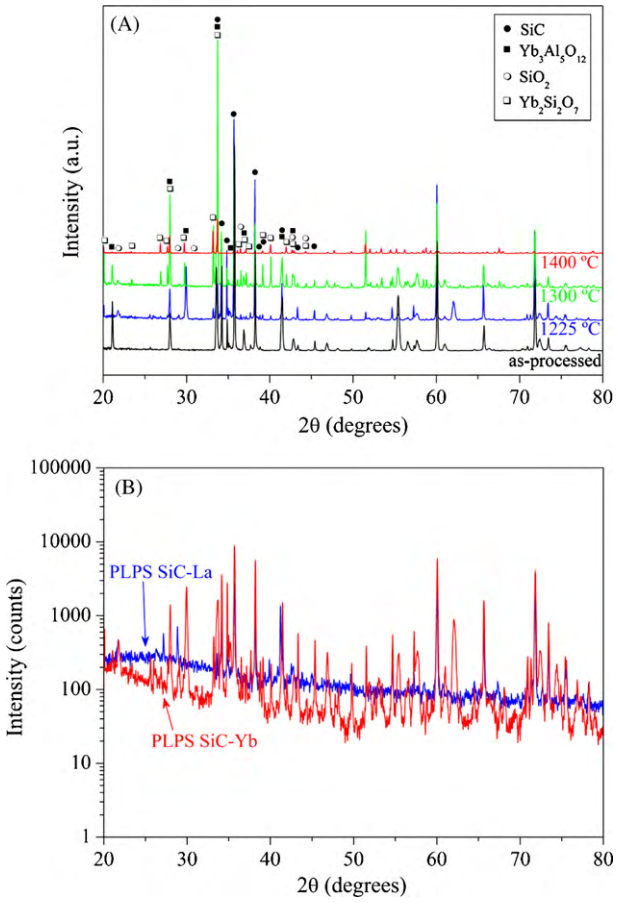

Fig. 8. XRD patterns of: (A) PLPS SiC–Yb at the as-processed condition and after oxidation in oxygen for 22 h at the different oxidizing temperatures, and (B) PLPS SiC–Yb (Yb^{3+} radius 0.868 Å) and –La (La^{3+} radius 1.032 Å) oxidized at 1225 °C in oxygen for 22 h. In (A) the phase identification is shown only up to about 45° 2θ, and the origins of the XRD patterns have been shifted to facilitate their observation. In (B) the intensities of the XRD patterns are given in logarithm scale to facilitate the comparison.

crystalline phases is several orders of magnitude slower than through amorphous phases.[14] Indeed, the degree of crystallization could account for most of the several orders of magnitude differences in the oxidation resistance between the ceramics with RE^{3+} cations of size inferior and superior to ~0.9 Å. With respect to the increased refractoriness of the crystalline silicates and the greater viscosity of the residual silicate liquid, earlier studies have shown that in rare-earth silicates these high-temperature properties are dictated by the field strength of the RE^{3+}–O^{2-} bond because this is the weakest bond in the structure.[19–23] Since this field strength is inversely proportional to the square of the RE^{3+} cation size,[24,b] one concludes that the crystalline silicates are more refractory and the silicate liquid more viscous as the size of the RE^{3+} cation decreases. These two effects also assist in increasing the oxidation resistance of the PLPS SiC by making oxygen diffusion through the oxide scale slower. Indeed, the refractoriness of the crystals and the viscosity of the amorphous residual phase could account for the most of the differences in the oxidation resistance between PLPS SiC–Yb, –Tm, –Er, and –Y, and between PLPS SiC–Nd and –La.

The present study thus confirms that reduction of the size of the RE^{3+} cation in the RE_2O_3 sintering aid is another processing strategy to improve the oxidation resistance of PLPS SiC, together with that already identified of the choice of sintering atmosphere of Ar or N_2[11] and the reduction of the intergranular phase content.[15] Furthermore, the present study presents the first evidence that RE_2O_3 with RE^{3+} cations of sizes above ~0.9 Å should never be used as sintering aids if PLPS SiC is to be used in an oxidizing atmosphere due to the severe degradation in oxidation resistance. Finally, another interesting implication of this study is that Y_2O_3 is a good candidate additive for oxidation-resistance applications below 1200 °C because at these temperatures it offers protection comparable to that of other RE_2O_3's with smaller cations but at considerably lower cost.

To conclude, it is important to mention that this was a study of short-term oxidation behaviour. Nevertheless, the observed dependence of oxidation resistance on the size of the RE^{3+} cation will still hold for long-term oxidation, although the rate-limiting mechanism of the oxidation may change to inward diffusion of oxygen through the oxide scale,[10,11] with the attendant changes in the activation energies of the oxidation.

5. Conclusions

The influence of the $5Al_2O_3 + 3RE_2O_3$ (RE = La, Nd, Y, Er, Tm, or Yb) sintering-additive on the oxidation behaviour of PLPS SiC was investigated. The following conclusions can be drawn from the results:

1. The oxidation of the PLPS SiC–RE ceramics at these temperatures is passive and protective, and its kinetics is given by the arctan-rate law. This type of oxidation is due to the formation of continuous oxide scales that crystallize progressively during the exposure to the oxidizing atmosphere.
2. The oxidation is in all cases controlled by outward diffusion of RE^{3+} cations from the secondary intergranular phase into the oxide scale. However, the activation energy of the oxidation decreases as the size of the RE^{3+} cation in the RE_2O_3 decreases, which is due to the easier diffusion of smaller cations.
3. The oxidation resistance of PLPS SiC increases as the size of the RE^{3+} cation in the RE_2O_3 decreases, an effect that is especially marked above ~0.9 Å where the oxidation rate decreases by several orders of magnitude. This trend is attributable to synergy of formation of oxide scales that are highly crystalline and that in addition contain crystals that are more refractory and amorphous residual phases that are more viscous.
4. Selection of RE_2O_3 sintering additives with cations as small as possible below 0.9 Å emerges as a design strategy of PLPS SiC for oxidation-resistance applications. RE^{3+} cations larger than 0.9 Å should not be used to process PLPS SiC if oxi-

[b] The field strength is given by $Z_aZ_ce^2/r^2$, where Z_a and Z_c are the charge of the anion and cation, respectively, e is the elementary electric charge, and r is the sum of the cationic and anionic radii.

dation during service is an important concern. In any case, Y_2O_3 is a good candidate additive if the upper-use temperature is below 1200 °C because its protection against oxidation is similar to that of other RE_2O_3's with smaller cations while its cost is considerably lower.

Acknowledgment

This work was supported by the Ministerio de Ciencia y Tecnología (Government of Spain) under Grant No. MAT 2007-61609.

Appendix A.

The objective of this Appendix is to show how the arctan-rate law (see Eq. (1)) can be derived. Essentially, the arctan-rate law is a modification of the parabolic-rate law for when the amorphous cross-section available for diffusion decreases progressively during oxidation. Thus, a mathematical function $A(t)$ describing the time dependence of this decrease is incorporated into the parabolic-rate law:

$$\frac{d(\Delta m_s)}{dt} = \frac{\sqrt{K_p}A(t)}{2\sqrt{t}} \tag{A1}$$

Consider that f is the fraction of original area ($0 \leq f \leq 1$) that still remains amorphous at a certain oxidizing time t_0 for which a steady state is reached where the amorphous cross-section available for diffusion does not longer decrease. To ensure that the new rate law reproduces the oxidation curves and has physical meaning, $A(t)$ cannot be chosen arbitrarily but must have necessarily at least the following mathematical properties: (i) $A(t)$ has to be equal to 1 at $t = 0$, and has to decrease to f at $t = t_0$; (ii) $A(t)$ has to be equal to 1 for all t if $f = 1$ so Eq. (1) yields the parabolic-rate law; and (iii) $A(t)$ has to be continuous and derivable. Empirically this function has been found to be:

$$A(t) = \frac{1 + (f\beta - t_0^{-1})t}{1 + (\beta - t_0^{-1})t} \tag{A2}$$

where β is the rate constant for the decrease of the area. Substitution of Eq. (A2) into Eq. (A1) and subsequently integration yields the arctan-rate law (see Eq. (1)).

Appendix B.

The aim of this appendix is to describe the fitting protocol followed to ensure that the modelling of the oxidation curves by the arctan-rate law converges in physically meaningful values. First of all, estimates of k_p and f were obtained; k_p was estimated by fitting the parabolic-rate law $\Delta m_s = (k_p t)^{1/2}$ to the oxidation curve, while f was estimated independently by image analysis from the direct measurement of the residual amorphous fraction in the SEM images. With this information, the fits were implemented in two stages. Initially k_p and f were fixed to the values estimated as described before, and β and t_0 were refined by the non-linear least squares method until convergence taking $b = 0$ because the oxidation curves were all previously corrected by the baseline drift. Thus, this first fitting stage essentially allowed β and t_0 to be estimated. Next, k_p, f, β and t_0 were all refined simultaneously by the non-linear least squares method until convergence, applying restraints on f to allow only 10% of variation with respect to value measured by SEM. The fits were conducted iteratively using both the Levenberg–Marquartd and simplex algorithms to ensure that they do not become trapped in local minima. In this way, four parameters are refined on the base of experimental curves with more than 4700 data, which in addition extended sufficiently over the time range as to enable sensible determination of these parameters. Thus, from the mathematical point of view the fits are well-defined. In addition, although no correlation is expected between the adjustable parameters, the fitting strategy employed would avoid the occurrence of mathematical artifacts in the determination of k_p, f, β and t_0. For example, in all cases it was observed that f converged within its interval of variation without reaching the limits, and that k_p deviated more from the estimate of the parabolic model as the f value decreased.

References

1. Zhou Y, Hirao K, Toriyama M, Yamauchi Y, Kanzaki S. Effects of intergranular phase chemistry on the microstructure and mechanical properties of silicon carbide ceramics densified with rare-earth oxide and alumina additives. *J Am Ceram Soc* 2001;**84**(7):1642–4.
2. Zhou Y, Hirao K, Yamauchi Y, Kanzaki S. Tailoring the mechanical properties of silicon carbide ceramics by modification of the intergranular phase chemistry and microstructure. *J Eur Ceram Soc* 2002;**22**(14–15):2689–96.
3. Liu D-M. Oxidation of polycrystalline α-silicon carbide ceramic. *Ceram Int* 1997;**23**(5):425–36.
4. Jensen RP, Luecke WE, Padture NP, Wiederhorn SM. High-temperature properties of liquid-phase-sintered α-SiC. *Mater Sci Eng* 2000;**A282**(1–2):109–14.
5. Biswas K, Rixecker G, Aldinger F. Improved high temperature properties of SiC–ceramics sintered with Lu_2O_3-containing additives. *J Eur Ceram Soc* 2003;**23**(7):1099–104.
6. Guo S, Hirosaki N, Tanaka H, Yamamoto Y, Nishimura T. Oxidation behavior of liquid-phase sintered SiC with AlN and Er_2O_3 additives between 1200 °C and 1400 °C. *J Eur Ceram Soc* 2003;**23**(12):2023–9.
7. Biswas K, Rixecker G, Aldinger F. Effect of rare-earth cation additions on the high temperature oxidation behavior of LPS–SiC. *Mater Sci Eng* 2004;**A374**(1–2):56–63.
8. Suzuki K, Kageyama N, Kanno T. Improvement in the oxidation resistance of liquid-phase-sintered silicon carbide with aluminum oxide additions. *Ceram Int* 2005;**31**(6):879–82.
9. Weidenmann KA, Rixecker G, Aldinger F. Liquid phase sintered silicon carbide (LPS–SiC) ceramics having remarkably high oxidation resistance in wet air. *J Eur Ceram Soc* 2006;**26**(13):2453–7.
10. Rodríguez-Rojas F, Borrero-López O, Ortiz AL, Guiberteau F. Oxidation kinetics of pressureless liquid-phase-sintered α-SiC in ambient air at elevated temperatures. *J Mater Res* 2008;**23**(6):1689–700.
11. Rodríguez-Rojas F, Ortiz AL, Borrero-López O, Guiberteau F. Effect of Ar or N_2 sintering atmosphere on the high-temperature oxidation behaviour of pressureless liquid-phase-sintered α-SiC in air. *J Eur Ceram Soc* 2010;**30**(1):119–28.
12. Choi H-J, Lee J-G, Kim Y-W. Oxidation behaviour of liquid-phase sintered silicon carbide with aluminum nitride and rare-earth oxides (Re_2O_3, where Re = Y, Er, Yb). *J Am Ceram Soc* 2002;**30**(1):2281–6.
13. Xu H, Bhatia T, Deshpande SA, Padture NP, Ortiz AL, Cumbrera FL. Microstructural evolution in liquid-phase-sintered SiC: Part I, effect of starting powder. *J Am Ceram Soc* 2001;**84**(7):1578–84.

14. Nickel KG. Corrosion of advanced ceramics. Measurement and modelling. NATO ASI series, series E (applied sciences), vol. 267; 1994.
15. Rodríguez-Rojas F, Ortiz AL, Borrero-López O, Guiberteau F. Effect of the sintering additive content on the non-protective oxidation behaviour of pressureless liquid-phase-sintered α-SiC in air. *J Eur Ceram Soc* 2010;**30**(6):1513–8.
16. Persson J, Nygren M. The oxidation kinetics of β-sialon ceramics. *J Eur Ceram Soc* 1994;**13**(5):467–84.
17. Lamkin MI, Riley FL, Fordham RJ. Oxygen mobility in silicon dioxide and silicate glasses: a review. *J Eur Ceram Soc* 1992;**10**(5):347–67.
18. Mehrer H. *Diffusion in solid metals and alloys*. Springer-Verlag; 1990.
19. Shelby JE, Kohli JT. Rare-earth aluminosilicate glasses. *J Am Ceram Soc* 1990;**73**(1):39–42.
20. Choi H-J, Lee J-G, Kim Y-W. High temperature strength and oxidation behaviour of hot-pressed silicon nitride-disilicate ceramics. *J Mater Sci* 1997;**32**(7):1937–42.
21. Cinibulk MK, Thomas G, Johnson SM. Oxidation behavior of rare-earth disilicate-silicon nitride ceramics. *J Am Ceram Soc* 1992;**75**(8):2044–9.
22. Ohashi M, Nakamura K, Hirao K, Kanzaki S, Hampshire S. Formation and properties of Ln–Si–O–N glasses (Ln = lanthanides or Y). *J Am Ceram Soc* 1995;**78**(1):71–6.
23. Ramesh R, Nester F, Pomeroy MJ, Mampshire S. Formation of Ln–Si–Al–O–N glasses and their properties. *J Eur Ceram Soc* 1997;**17**(15–16):1933–9.
24. Dietzel A. The cation field strengths and their relation to devitrifying process to compound formation and to the melting points of silicates. *Z Elektrochem* 1942;**48**(1):9–23.